Reactive boride infusion stabilizes Ni-rich cathodes for lithium-ion batteries

Citation: Yoon, Moonsu, Dong, Yanhao, Hwang, Jaeseong, Sung, Jaekyung, Cha, Hyungyeon et al. 2021. "Reactive boride infusion stabilizes Ni-rich cathodes for lithium-ion batteries." Nature Energy, 6 (4).

As Published: 10.1038/S41560-021-00782-0

Publisher: Springer Science and Business Media LLC

Persistent URL: https://hdl.handle.net/1721.1/141024

Version: Author's final manuscript: final author's manuscript post peer review, without publisher's formatting or copy editing

Reactive boride infusion stabilizes Ni-rich cathodes for lithium-ion batteries

Moonsu Yoon[1,†], Yanhao Dong[2,†], Jaeseong Hwang[1], Jaekyung Sung[1], Hyungyeon Cha[1], Kihong Ahn[1], Yimeng Huang[3], Seok Ju Kang[1], Ju Li[2,3,*], Jaephil Cho[1,*]

[1]*School of Energy and Chemical Engineering, Ulsan National Institute of Science and Technology (UNIST), 50 UNIST-gil, Ulsan 44919, Republic of Korea*

[2]*Department of Nuclear Science and Engineering, Massachusetts Institute of Technology, Cambridge, Massachusetts 02139, United States*

[3]*Department of Materials Science and Engineering, Massachusetts Institute of Technology, Cambridge, Massachusetts 02139, United States*

†: Equal contribution.

*Corresponding authors. Email: liju@mit.edu (J.L.), jpcho@unist.ac.kr (J.C.).

Abstract

Engineered polycrystalline electrodes are critical to the cycling stability and safety of lithium-ion batteries, yet it is challenging to construct high-quality coatings at both the primary- and secondary-particle levels. Here, we present a room-temperature synthesis route to achieve full surface coverage of secondary particles and facile infusion into grain boundaries, thus offering a complete "coating-plus-infusion" strategy. Cobalt boride metallic glass is successfully applied to Ni-rich layered cathode $LiNi_{0.8}Co_{0.1}Mn_{0.1}O_2$. It dramatically improves the rate capability and cycling stability, including under high-discharge-rate and elevated-temperature conditions and in pouch full cells. The superior performance originates from simultaneous suppression of microstructural degradation of intergranular cracking and side reactions with electrolyte. Atomistic simulations identified the critical role of strong selective interfacial bonding, which offers not only a large chemical driving force to ensure uniform reactive wetting and facile infusion but also lowered the surface/interface

oxygen activity, contributing to the exceptional mechanical and electrochemical stabilities of the infused electrode.

Introduction

Future energy infrastructure seeks advanced cathode active materials for lithium-ion batteries (LIBs) with higher energy and power density, longer cycle life and better safety[1-3], whereas high-voltage and high-rate cycling often triggers accelerated degradation, premature failure, and safety issues[4, 5]. Many efforts have been spent on exploring new cathode chemistry, introducing dopants into the bulk and at the surface, and designing nano-/micro-/hetero-structures[6-8]. Coating is a widely exercised method to improve cathode stability, which can work synergistically with other cathode modifications[9-11]. While a thin coating with high stability and catalytic inertness is helpful, it is often difficult to achieve 100% coverage in synthesis due to solid-on-solid wetting problem and to remain conformal during electrochemical cycling. These challenges set the motivation for the present work, which utilizes a simple liquid-solution method to construct high-quality cathode coating by reactive wetting with the oxide active material.

We choose a Ni-rich layered cathode $LiNi_{0.8}Co_{0.1}Mn_{0.1}O_2$ (NCM or NCM811) of significant industrial interest as a model system to demonstrate our coating strategy. During electrochemical cycling of NCM, a series of detrimental processes take place, including phase transformation in the bulk and at the surface[12], intergranular cracking of the secondary particles along grain boundaries (GBs)[13, 14], formation and growth of cathode electrolyte interphases (CEIs)[15], and side reactions consuming precious liquid organic electrolytes that also generate gases and cause transition metal (TM) dissolution (which may later migrate and precipitate at the anode side and affect the anode stability)[16-18]. The above processes result in continuous impedance growth and degrade the full-cell performance, especially under high-rate conditions. One key issue is the stability of surface oxygen, which becomes labile at high voltages and easily escapes. Such oxygen loss not only oxidizes organic electrolytes and evolves gases, but also leads to cation reduction/densification[19] and phase transformations[20, 21], which may in turn initiate other degradation processes in a chain-reaction manner[22-24]. In this sense, it is beneficial to construct a coating that binds strongly with the surface oxygen to address the root-cause of the high-voltage instability.

We selected a cobalt boride (Co_xB) coating with the following considerations: First, Co_xB is a metallic compound that has no direct tie-lines with oxygen[25] and thermodynamically it would react with oxygen to form stable compounds such as B_2O_3, Co_3O_4 and $Co_4B_6O_{13}$, implying strong reactivity between Co_xB and the surface oxygen of NCM. Second, Co_xB has an exceptional oxidation resistance even at elevated temperatures (850-950°C)[26]. This means even though Co_xB likes to react with oxygen, the reaction is kinetically self-limiting, likely due to the glass-forming ability of the B_2O_3-like product at the interface that forms a compact self-healing passivation layer[27, 28]. Thus, while the reactive wetting ensures complete coverage and tight adhesion between the Co_xB and NCM, it does not consume much oxygen from NCM lattice and will likely maintain a metallic glass nature[29, 30]. The passivation would kinetically suppress oxygen penetration/loss through this coating layer, and the interfacial polyanionic borate glass also incorporates Li alkali metal that comes with NCM, making itself a mixed ionic and electronic conductor (MIEC). Third, Co_xB coating can be synthesized at room temperature[31, 32], which eliminates the necessity of follow-up high-temperature treatments that may introduce additional complexity to the heavily optimized synthesis route of NCM. Forth, cobalt boride has been used to coat metal parts to improve their corrosion and wear resistance, thus its mechanical properties should be good in the sense that it must not easily chip or fracture at nanoscale. Remarkably, we shall show that the as-synthesized Co_xB coating not only completely covers the surface of NCM secondary particles, but also infuses into the GBs between primary particles with zero equilibrium wetting angle, which we shall abbreviate as "infusion" to distinguish it from typical surface coating. This is similar to the complete wetting of GBs by liquid metal (e.g., liquid Ga in aluminum GBs), and intergranular amorphous nanofilms in ceramics. The infused microstructure (**Fig. 1**) dramatically improves the rate capability and cycling stability of NCM, including under high-discharge-rate (up to 1,540 mA g^{-1}) and high-temperature (45°C) conditions, by greatly suppressed intergranular cracking, side reactions and impedance growth.

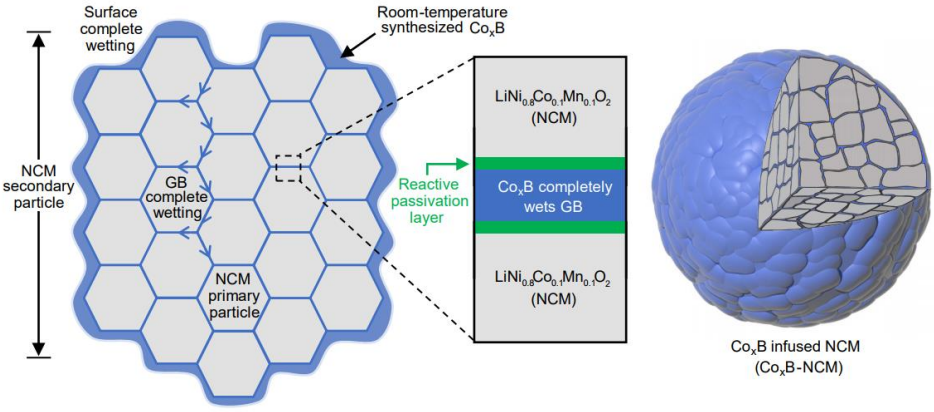

Figure 1 | "Coating-plus-infusion" microstructure for Co_xB infused NCM. Schematic "coating-plus-infusion" microstructure where Co_xB uniformly coats the surface of NCM secondary particle and infuses into GBs between NCM primary particles.

Co_xB fully covers NCM surface and infuses into GBs

Pristine NCM was synthesized by a co-precipitation technique, followed by calcination with lithium hydroxide in a flowing oxygen atmosphere. To obtain Co_xB infused NCM (Co_xB-NCM), pristine NCM was added into the ethanol solution of $Co(NO_3)_2$, followed by the addition of ethanol solution of $NaBH_4$ at room temperature under argon protection. Co_xB-NCM was then washed, collected and dried (see Methods and **Supplementary Fig. 1**). Using inductive coupled plasma optical emission spectrometry (ICP-OES, **Supplementary Table 1**), we confirmed the infused Co_xB has a composition close to $Co_{2.2}B$. Both pristine NCM and Co_xB-NCM have layered structure shown by X-ray diffraction (XRD) data in **Supplementary Fig. 2**, with minimum Ni/Li cation mixing (1.2% for pristine NCM811 and 1.1% for Co_xB-NCM; Rietveld refinement data in **Supplementary Table 2**).

The synthesized NCM has a typical polycrystalline microstructure with spherical secondary particles (D_{50} ~12 μm; **Supplementary Table 3**) consisting of fine-grained primary particles (**Fig. 2a**). Such a microstructure is well maintained in Co_xB-NCM (**Fig. 2b**), where a continuous uniform coating with a nano-scale fuzzy morphology can be found at the surface under both scanning electron microscope (SEM, **Fig. 2b**; more examples in **Supplementary Fig. 3**) and transmission electron microscope (TEM, **Fig. 2c**, **d**; the fuzzy morphology has a meso-porous structure as confirmed by the pore size distribution in **Supplementary Fig. 4**). We found the coating layer at the

surface of crystalline NCM is amorphous with ~5 nm thickness (**Fig. 2c**; coating layer identified by the contrast as shown in **Supplementary Fig. 5**). It is enriched in Co and B and depleted in Ni and O compared to the NCM lattice from energy dispersive X-ray spectroscopy (EDS) mapping (**Fig. 2e**), consistent with the targeted Co_xB composition. Remarkably, despite the room-temperature synthesis route and the lack of high-temperature annealing, Co_xB infuses into the GBs between the NCM primary particles as shown by the EDS mapping in **Fig. 2f**, and it completely wets the GBs with equivalent contact angle of zero degree. More examples of TEM-EDS mapping in **Supplementary Fig. 6-8** confirmed the uniform surface coverage and infusion into the GBs deep inside the secondary particles up to >2–3 μm, which gives an unusually large room-temperature diffusivity of 1.4×10^{-16}–3.1×10^{-16} m^2 s^{-1} for Co_xB species if estimated from two-dimensional random walk model. It thus indicates a huge driving force for 2D diffusion/penetration and supports a reactive wetting process, where the coating layer spreads over the surface and GBs of the matrix driven by chemical reactions at the interface.

Benefiting from such reactive wetting, we found Co_xB completely covers the surface of NCM, as supported by X-ray photon spectroscopy (XPS) data in **Fig. 2g-n** (fitting details in **Supplementary Table 4**): Compared to pristine NCM, Co_xB-NCM shows not only strong B 1*s* signal around 187.8 eV (**Fig. 2g**, absent in pristine NCM in **Fig. 2k**)[31, 33] and negatively shifted Co $2p_{3/2}$ signal around 778.5 eV (**Fig. 2h**, vs. 780.2 eV for Co^{3+} $2p_{3/2}$ signal in pristine NCM in **Fig. 2l**; unlike Co^{3+} in NCM, Co_xB is metallic with Co peaks shifting towards lower binding energy)[34], but also hugely suppressed Ni 2*p*, and Mn 2*p* signals (**Fig. 2i&j**, vs. strong signals in pristine NCM in **Fig. 2m&n**)[35]. Because XPS is a surface-sensitive technique, the absence of Ni and Mn signals suggests a complete coverage of Co_xB coating layer at the surface of NCM particles (so that the XPS signals are mainly contributed by the coating layer), with much better statistics than typical TEM characterizations.

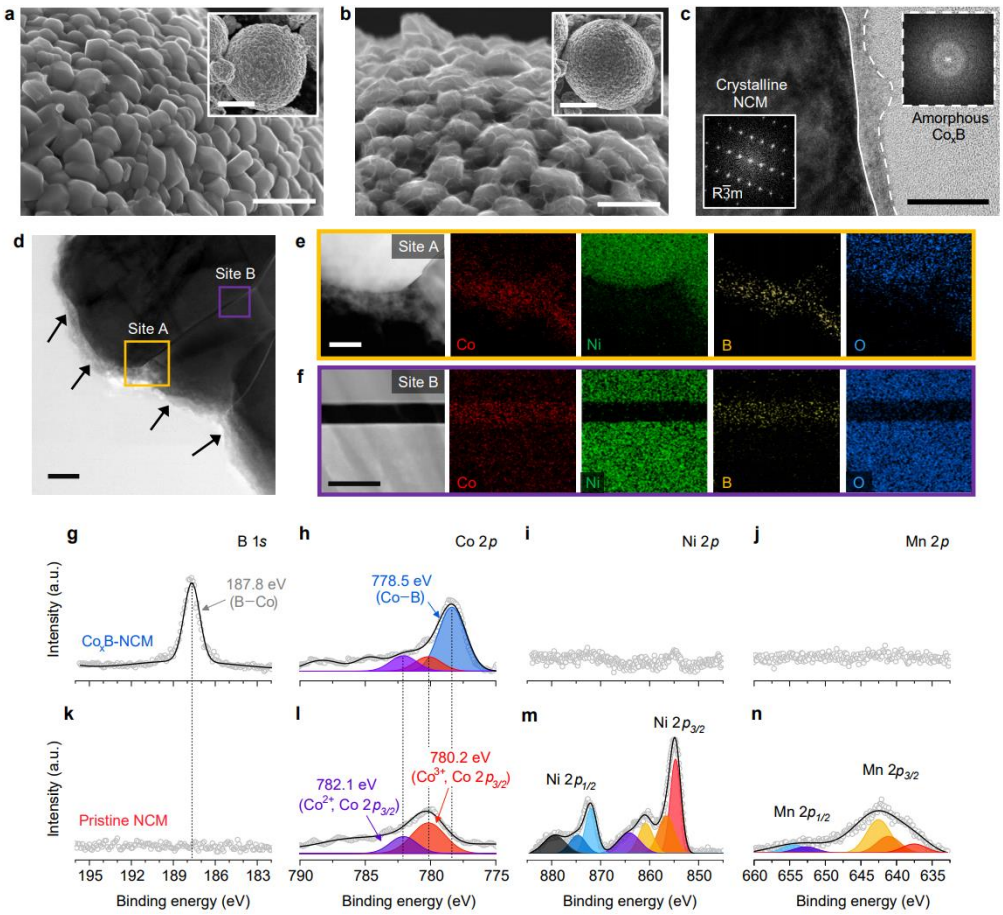

Figure 2 | Uniform amorphous Co$_x$B infusion at NCM surface and grain boundaries. SEM images of (a) pristine NCM and (b) Co$_x$B-NCM. Insets of (a-b): Lower-magnification SEM images showing morphology of NCM secondary particles. (c-d) TEM image of cross-sectioned Co$_x$B-NCM near the surface. Insets of (c): FFT patterns showing crystalline NCM and amorphous Co$_x$B. (e) EDS mapping of site A in (d). (f) EDS mapping of site B in (d). Scale bars: 1 μm in (a-b), 5 μm in insets of (a-b), and 20 nm in (c-f). XPS spectra of B 1*s*, Co 2*p*, Ni 2*p* and Mn 2*p* for Co$_x$B-NCM (g-j) and pristine NCM (k-n). Details for XPS data analysis are listed in **Supplementary Table 4**.

Enhanced rate capability and cycling stability

We next investigated the electrochemical performance of pristine NCM and Co$_x$B-NCM as LIB cathodes in coin-type half cells under high loading (10.5±0.2 mg cm^{-2}, corresponding to an areal capacity of ~2.05 mAh cm^{-2}) and high electrode density (3.20±0.03 g cm^{-3}). When firstly charged/discharged at 0.1 C (1 C defined as 220 mA g^{-1}) between 3.0 V and 4.4 V vs. Li/Li$^+$ at 25°C, pristine NCM and Co$_x$B-NCM show similar charge-discharge curve, discharge capacity around 215 mAh g^{-1} and first-cycle Coulombic efficiency (CE) around 91.5%, and their redox behaviors are similar shown by dQ/dV analysis (**Supplementary Figs. 9a, b**). However, Co$_x$B-NCM has better rate capability (**Fig. 3a**, **b**) and cycling stability (shown by 1 C cycling data performed after the rate

tests in **Fig. 3a** and 0.5 C cycling data in **Supplementary Fig. 10**). To gain better understanding of the improved rate capability and cycling stability, we conducted galvanostatic intermittent titration technique (GITT) measurements with a titration current of 0.5 C after the first (41^{st} cycle in total number of cycling) and last (140^{th} cycle in total number of cycling) cycles of 1 C cycling in **Fig. 3a**. As shown by the discharge profiles in **Fig. 3c**, more severe polarization develops in cycled pristine NCM than in cycled Co_xB-NCM and the average voltage loss is 3.75 times larger in the former. More detailed GITT analysis in **Supplementary Fig. 11** demonstrates minimum impedance growth in cycled Co_xB-NCM and huge impedance growth in pristine NCM mostly in the form of ohmic loss (indicating degraded electron transport at the electrode level which is consistent with observed intergranular cracking to be discussed later), which are further supported by electrochemical impedance spectroscopy (EIS) measurements in **Supplementary Fig. 12**.

To highlight the exceptional performance offered by Co_xB infusion, we tested under harsher conditions with 7 C discharge rate at 45ºC (note the cells were charged at 0.5 C because lithium metal anode cannot afford such a fast charging rate). While pristine NCM rapidly fades within 60 cycles, Co_xB-NCM can be stably cycled up to 200 cycles with a capacity retention of 82.2%, high CE (**Fig. 3d**), high energy efficiency and stable average discharge voltage (**Supplementary Fig. 13a-d**). The rapid failure of pristine NCM in 7 C-discharge cycling is due to the kinetic reason of impedance over-growth instead of thermodynamic transformation, since the intermittent recovery step (conducted after every 100 cycles with slow charge/discharge rate of 0.2 C) can recover most of the capacity as shown in **Fig. 3d**. The conclusion is further supported by EIS data measured after different 7 C-discharge cycles in **Supplementary Fig. 14**, which shows dramatical impedance growth of pristine NCM upon cycling. Additional experiments were conducted with 5 C discharge rate at 45ºC (**Supplementary Fig. 15**), which again demonstrates the superior performance of Co_xB-NCM. Lastly, we tested pristine NCM and Co_xB-NCM in 400 mAh pouch-type full cells using spherical graphite (Gr) anode and conducted long-term cycling in the voltage range of 2.8−4.3 V at 25°C. As shown in **Fig. 3e**, Co_xB-NCM has an impressive capacity retention of 95.0% (vs. 79.2% for pristine NCM) and high CE at 1.0 C/1.0 C charge/discharge for 500 cycles (more detailed electrochemical performances in **Supplementary Fig. 16**). Therefore, Co_xB infusion can greatly enhance rate capability and cycling stability of NCM with suppressed impedance growth and voltage loss, especially under high-rate and high-temperature conditions.

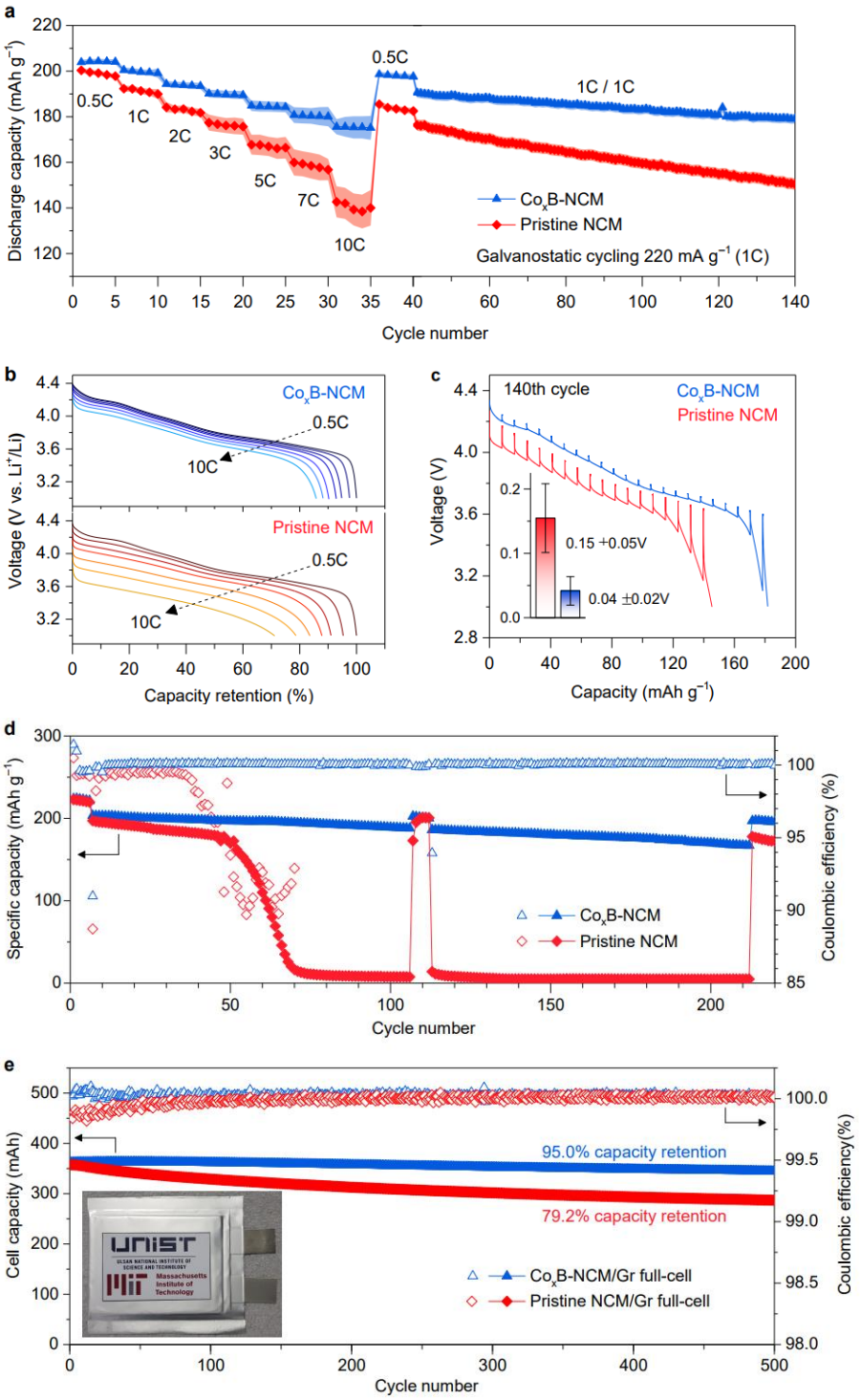

Figure 3 | Superior electrochemical performance of Co$_x$B-NCM over pristine NCM. (a) Rate tests and 1 C cycling of Co$_x$B-NCM and pristine NCM in the voltage range of 3.0−4.4 V vs. Li/Li$^+$ at 25ºC. Shaded region in (a) is the standard deviations calculated from five cells. (b) Discharge curves at different rates. (c) Discharge curves of GITT measurements conducted after 140th cycle in (a). Inset of (c): average voltage loss and its standard deviation (raw data available in **Supplementary Fig. 11**) over different GITT steps. (d) 7 C-discharge cycling tests in the voltage range of 3.0−4.4 V vs. Li/Li$^+$ at 45ºC, where 6 intermittent cycles with 0.2 C charge/discharge were conducted after every 100 cycles. (e) Cycling performance of Co$_x$B-NCM/Gr and pristine NCM/Gr

full cells at 1.0 C in the voltage range of 2.8−4.3 V at 25°C. Inset of (e): Photo of an assembled pouch cell.

Mitigating microstructural degradation and side reactions

Pristine NCM and Co_xB-NCM show dramatically different microstructures after cycling. After 200 cycles under 7 C discharge rate at 45°C, we observed severe intergranular cracking in pristine NCM as shown by TEM in **Fig. 4a** and SEM in **Supplementary Fig. 17a**, **b**, which creates more electrolyte-exposing fresh surfaces and leads to extensive CEI formation as indicated by EDS mapping of F and C both at the surface and inside the secondary particle (insets of **Fig. 4a**). In comparison, the secondary particles of Co_xB-NCM remain intact without cracking as confirmed by TEM (**Fig. 4d**) and SEM (**Supplementary Fig. 17c**, **d**), and F and C signals are weaker (insets of **Fig. 4d**), suggesting less electrolyte infiltration and CEI formation[36]. Similarly suppressed cracking by Co_xB infusion is also observed in firstly charged cathodes as well as the ones after 500 cycles in pouch cells (**Supplementary Figs. 18, 19**). The contrasting cracking behaviors are interesting because intergranular cracking of Ni-rich cathodes was typically attributed to anisotropic lattice expansion/shrinkage and heterogeneous charge/discharge kinetics during electrochemical cycling[37, 38], which can hardly be removed by cathode coating. Indeed, as shown by *in situ* XRD during electrochemical cycling (**Supplementary Figs. 20, 21**), pristine NCM and Co_xB-NCM undergo the same bulk phase transformation and lattice expansion/shrinkage (**Supplementary Fig. 22**). Similar observations have also been recently reported in the literature where appropriate cathode coatings and electrolyte compositions can efficiently reduce intergranular cracking[10, 39, 40]. Therefore, large-scale cracking cannot be solely driven by mechanical stress/strain alone; instead, it should also involve side chemical reactions at the GBs, in other words being a stress-corrosion cracking (SCC) problem.

The hypothesis is supported by simultaneously suppressed side reactions and surface phase transformations by Co_xB infusion. To demonstrate the correlation, we firstly characterized the fresh surface generated by intergranular cracking in cycled pristine NCM under TEM (**Fig. 4b**), which shows a thick (~13 nm) cation-mixed rock-salt phase (originated from surface oxygen loss followed by surface cation densification). From electron energy loss spectroscopy (EELS) measurements in **Fig. 4c** and **Supplementary Fig. 23a**, we found severe transition metal reduction (Ni^{3+} reduced to Ni^{2+} shown by Ni L_3 edge) and defects in oxygen sublattice (shown by O K edge) near the surface

of cycled pristine NCM[41, 42]. In comparison, for cycled Co_xB-NCM, we found thinner transformed cation-mixed rock-salt phase (~2 nm, **Fig. 4e**) even at the surface of secondary particles and much less Ni reduction and oxygen defects (**Fig. 4f**). The suppressed surface cation reduction, cation densification and surface phase transformation apparently benefit from Co_xB infusion, as the morphology and chemistry remain unchanged at both surfaces and GBs, confirmed by TEM in **Supplementary Fig. 23b**, **24**, and **25a**, and EDS in **Supplementary Fig. 24d** and **25b**.

Second, the surfaces of cycled samples were characterized by XPS, where stronger signals of C 1*s* (contributed by organic CEI components like polycarbonates and semicarbonates)[40, 43, 44], F 1*s* (contributed by CEI components of metal fluorides like NiF_2 and LiF), and Ni 2*p* signals (contributed by Ni-containing CEI components like NiF_2)[45] can be observed in cycled pristine NCM than in cycled Co_xB-NCM (**Fig. 4g-i**; see detailed discussions in **Supplementary Table 5**). Meanwhile, strong Co 2*p* and B 1*s* signals can be observed in cycled Co_xB-NCM, indicating the Co_xB surface coating is not covered by thick CEIs even after prolonged cycling. Both observations above suggest suppressed CEI growth in Co_xB-NCM (**Fig. 4j-k**).

Third, by *in situ* differential electrochemical mass spectrometry (DEMS) measurements in **Fig. 4l**, we found much less gas evolution (CO_2 and O_2) during the first charge cycle of Co_xB-NCM than that of pristine NCM. It suggests that Co_xB infusion effectively lowers the surface and GB oxygen activity and suppresses the electrolyte oxidation (The Co_xB infusion may also work by physically separating the electrolyte). Meanwhile, from ICP-OES measurements of the electrolytes in cycled cells in **Fig. 4m** and **Supplementary Table 6**, we found less TM dissolution (Ni, Co and Mn) in cycled Co_xB-NCM than in pristine NCM. Therefore, we conclude that our coating efficiently mitigates the side reactions between cathode and electrolyte as well as side reaction products in the solid (CEIs), gas (CO_2 and O_2) and soluble form (dissolved Ni, Co and Mn), and the suppressed side reaction correlates well with eliminated microstructural degradation, supporting the proposed mechanism of SCC retardation.

Lastly, the boride infusion treatment improves safety as demonstrated by differential scanning calorimetry (DSC) in **Supplementary Fig. 26**. The exothermal reaction in 4.4 V (vs. Li/Li^+) charged Co_xB-NCM takes place at higher temperature of 269.5ºC with less heat generation of 487.9 J g^{-1}, compared to 250.9ºC and 786.3 J g^{-1} for 4.4 V charged pristine NCM, respectively. This is a strong proof of the chemical passivation kinetics we postulated, since oxygen release during cathode

thermal decomposition is an important step in the exothermic reaction chain, and by reducing oxygen release, Co_xB-NCM is able to delay the thermal runaway and reduce the total heat released [46].

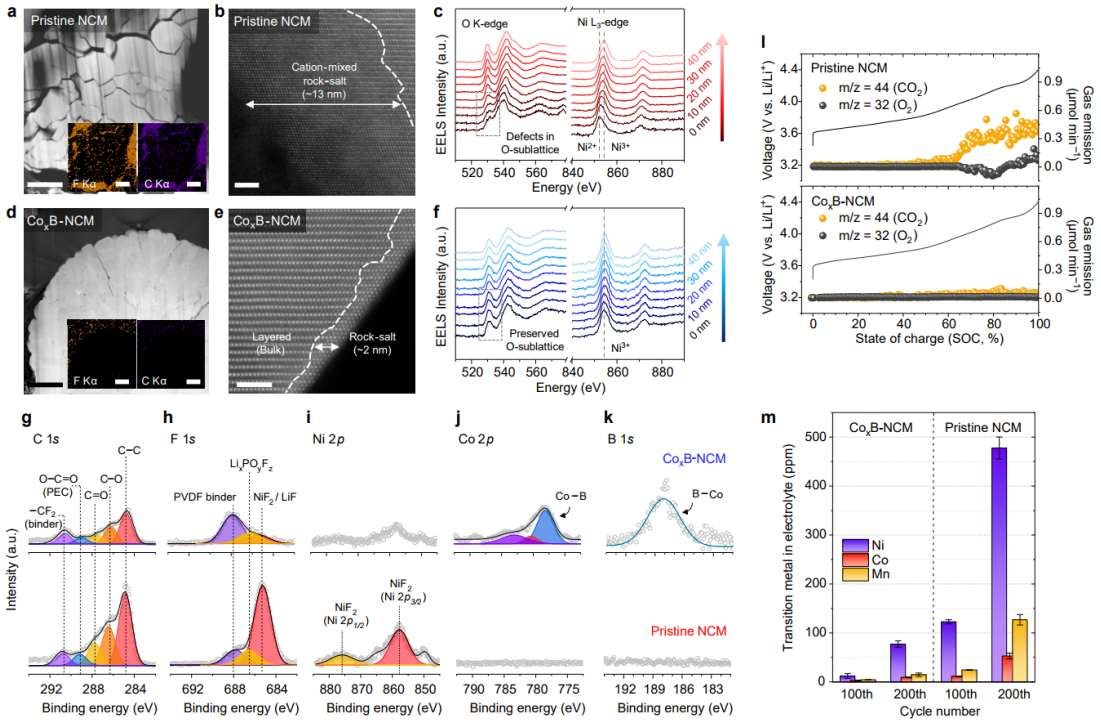

Figure 4 | Co_xB irrigation simultaneously suppresses microstructural degradation and side reactions. (a) TEM image and EDS mapping (inset) of pristine NCM after 200 cycles under 7 C discharge-rate at 45°C. (b) HR-TEM at fresh surface generated by intergranular cracking and (c) EELS line-scan at secondary-particle surface in cycled pristine NCM. (d) TEM image and EDS mapping (inset) of Co_xB-NCM after 200 cycles under 7 C discharge-rate at 45°C. (e) HR-TEM and (f) EELS line-scan at secondary-particle surface in cycled Co_xB-NCM. Scale bars: 2 μm in (a, d), and 2 nm in (b, e). (g-k) XPS spectra of C 1*s*, F 1*s*, Ni 2*p*, Co 2$p_{3/2}$, and B 1*s* for Co_xB-NCM (upper panel) and pristine NCM (lower panel) after 200 cycles under 7 C discharge-rate at 45°C. (l) *In-situ* DEMS data of pristine NCM and Co_xB-NCM during first charge at 0.2 C in the voltage range of 3.0−4.4 V vs. Li/Li^+ at 25ºC. (m) Dissolved Ni, Co and Mn in the electrolytes measured by ICP-OES after 100 and 200 cycles under 7 C discharge-rate at 45°C (Electrolytes from three different cells were measured to obtain the averages and standard deviations for each data point).

Cross-over effect on lithium metal anode

High-energy-density lithium metal batteries are currently under development[47] and we found the dissolved TMs from NCM cathode significantly affect the morphology and electrochemical performance of lithium metal anode (LMA) during the 7 C-discharge cycling at 45ºC. After 200 cycles, we found the surface of the LMA paired with pristine NCM became rough (**Fig. 5a**) with a porous layer consisting of mossy lithium and solid-electrolyte interphases (SEI) as shown in **Fig.**

5b. EDS mapping of the porous layer in **Fig. 5c** identified not only non-uniform C and F distributions, but also strong Ni signals enriched at the SEI/LMA interface, from the "cross-over" effect of Ni dissolution, migration, and deposition on the anode[9, 18]. In comparison, the LMA paired with Co_xB-NCM has a smooth surface and a dense SEI layer (**Fig. 5d,e**). The contrasting morphology is closely related to the composition and stability of the SEI, and by XPS measurements (**Fig. 5f**), we confirmed the SEI of the LMA paired with Co_xB-NCM indeed have much weaker Ni signals than the one paired with pristine NCM (Note Mn and Co are un-detectable as shown by XPS in **Supplementary Fig. 27** for cycled LMAs paired with both pristine NCM and Co_xB-NCM, probably due to lower dissolved concentrations in the electrolytes). Electrochemically, the deposited Ni-induced morphological instability would significantly degrade the performance of LMA, which is proved by the cycling experiments of Li/Li symmetric cells in **Supplementary Fig. 28**. Therefore, the suppressed TM dissolution by our coating conveys additional benefit by removing the cross-over effect on LMA and improves the full-cell cycling stability (**Supplementary Fig. 29**).

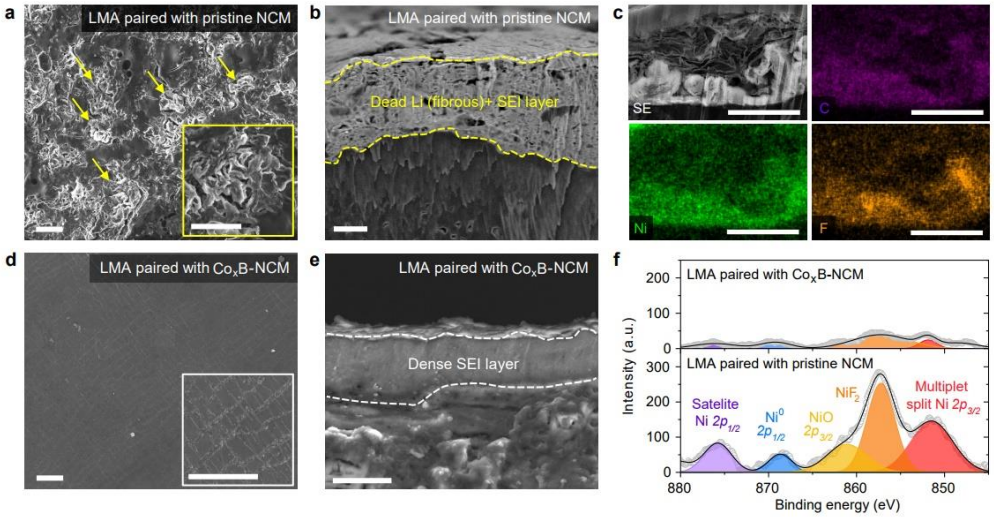

Figure 5 | Morphology and chemical characteristics of cycled lithium metal anode (LMA). (a) Top-view and (b) cross-sectional SEM images, and (c) EDS mapping of LMA paired with pristine NCM after 200 cycles under 7 C discharge-rate at 45°C. (d) Top-view and (e) cross-sectional SEM images of LMA paired with Co_xB-NCM after 200 cycles under 7 C discharge-rate at 45°C. Scale bars: 20 μm in (a, d), and 5 μm in (b, c, e). (f) XPS spectra of Ni 2*p* for Co_xB-NCM and pristine NCM after 200 cycles under 7 C discharge-rate at 45°C.

Selective interfacial bonding and suppressed oxygen activity

For atomistic details, first-principles calculations were conducted on the (104) surface of $LiNiO_2$ and on the interface between $LiNiO_2$ (104) surface and amorphous Co_xB. As shown by the relaxed

atomic structure of a $LiNiO_2$ slab with the top and bottom (104) surfaces in **Supplementary Fig. 30a**, the LiO_6 (in grey) and NiO_6 (in purple) octahedra are truncated at the surfaces, creating under-bonded surface oxygen with two kinds of local structures: type I coordinated by 2 Ni and 3 Li, and type II coordinated by 3 Ni and 2 Li. Note in the bulk of $LiNiO_2$, the lattice oxygen is always coordinated by 3 Ni and 3 Li (inset of **Supplementary Fig. 30b**), which promotes strong hybridization between Ni 3*d* and O 2*p* orbitals (with 3×Ni–O–Li local configurations) and lowers the energy level of occupied O 2*p* states (**Supplementary Fig. 30b**). However, the type I surface oxygen has a nil–O–Li configuration (in addition to 2×Ni–O–Li configurations; inset of **Supplementary Fig. 30c**), which indicates weaker Ni 3*d*–O 2*p* hybridization and creates more high-energy O 2*p* states close to the Fermi level E_F (**Supplementary Fig. 30c**). This is the origin of surface oxygen instability, which is prone to lose electrons at high voltages and subsequently evolves oxygen gases. Indeed, similar analyses have been put forward in Li-rich cathode materials[48,49], where Li–O–Li local configuration raises the electronic energy of O 2*p* states and is responsible for the observed oxygen redox.

At the interface between $LiNiO_2$ (104) surface and amorphous Co_xB (**Fig. 6a**), Co and B preferentially bond with surface O of $LiNiO_2$, but not with Li or Ni. The interfacial Co–O and B–O bonds are stronger than lattice Ni–O bond, as indicated by more electron cloud sharing for the former in the charge density plot (**Fig. 6b, c**). Note in **Fig. 6c**, the B–O bond has short bond distance (of 1.33 Å) and the electron cloud of O polarizes toward B, suggesting a covalent bonding nature. Considering the local structure, the type I "surface" O (now becoming an interfacial O) is coordinated either by 1 Co, 2 Ni and 3 Li (inset of **Fig. 6e**) or by 1 B, 2 Ni and 2 Li (inset of **Fig. 6f**; the strong B–O bond pulls O away from the center of the original "octahedral" site and the polyhedron becomes similar to a distorted square pyramid). Even though the O coordination in **Fig. 6e** is similar to that in the lattice (by 3 Ni and 3 Li, inset of **Fig. 6d**), the strong Co–O bond effectively lowers the energy of O 2*p* states (**Fig. 6e**), which have less high-energy states close to E_F than that of the lattice O (**Fig. 6d**). A more dramatical energy-level lowering is achieved by the strong covalent B–O bond as shown in **Fig. 6f**, which greatly stabilized the interface O. We further verified such an analysis approach on local structures is robust, as the same conclusion can be drawn from the amorphous Co_xB GB phases with different atomic structures (**Supplementary Fig. 31**). The above results clearly demonstrate that the chemical nature of reactive wetting is the selective

Co–O and B–O bonds formed at Co_xB/NCM interface, and the superior stability has an electronic-structure origin that effectively suppresses interface oxygen activity. This rationalizes the design of reactive-wetting metal-metalloid glass[29, 30] coating materials with selective bonding, which ensures not only uniform complete coverage but also stabilizing surface oxygen.

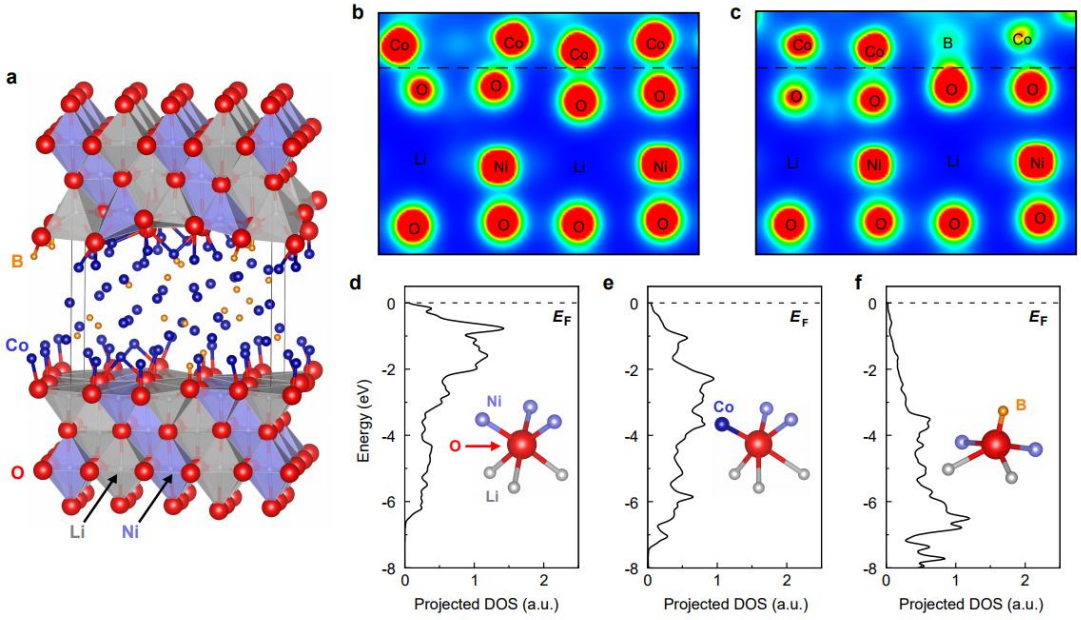

Figure 6 | Strong Co–/B–O interfacial bonding suppresses oxygen activity. (a) Atomic structure and (b-c) 2-dimensional slices of charge density distribution of simulated interface between $LiNiO_2$ (104) surface and amorphous Co_xB (dash lines denote the $Co_xB/LiNiO_2$ interface). Projected density of states (DOS) and schematic local environment (insets of d-f) of (d) lattice oxygen coordinated by 3 Ni and 3 Li, (e) interface oxygen coordinated by 1 Co, 2 Ni and 3 Li, and (f) interface oxygen coordinated by 1 B, 2 Ni and 2 Ni.

Regarding the improved mechanical stability, while Co_xB infusion mitigates SCC by stabilizing surface oxygen and suppressing the side reactions, it also benefits from a mechanical perspective, as less cracking was found even at the end of the first charge (**Supplementary Fig. 18**) when the chemical effect should be less conspicuous. Consistent with the strong interfacial bonds and reactive wetting, we found 4.6 times higher "opening" strength (41 GPa, **Supplementary Fig. 32**) in first-principles cohesive zone calculations at $Co_xB/LiNiO_2$ interface compared to that of bulk $LiNiO_2$ (9 GPa), which would help to suppress Mode I crack. For Mode II and III cracks, we suspect that the metallic glass Co_xB phase is shear-weak and can assist inelastic grain-boundary sliding via coordination-number preserving bond switching. This could be an effective way to release strain energy and avoid stress concentration at the GBs, thus benefiting the long-term mechanical integrity

(**Supplementary Fig. 19**). The above picture allows us to propose the design principles for reactive coating/infusion. For oxide cathodes that are synthesized under an oxidizing atmosphere, a reducing agent (an electron donor) would have strong affinity to surface oxygen. It applies to metallic compounds, especially borides/phosphides/silicides and alike which can form strong covalent bonds with surface oxygen, in other words creating interfacial polyanion groups that stabilize labile surface oxygen. The latter concept applied to the 3D lattice is exactly the one that led to the invention of polyanion LIB cathodes (e.g., $LiFePO_4$) with excellent stability and safety. Meanwhile, for the reactive wetting process to happen, such covalent bonds should be *in situ* formed at the interface and not pre-exist in the coating materials so that a large driving force can be derived from the interfacial chemical reactions. This means that while borides reactively wet oxide particles, borates cannot[50]. Regarding the synthesis route of the coating material, it may require a highly reducing condition, as in the present work where $NaBH_4$ was used. To minimize TM reduction at the interface (when NCM is treated with $NaBH_4$, slight reduction of Ni but not Co and Mn may occur at the surface as shown in **Supplementary Fig. 33**), a low synthesis temperature is thus preferable, such as room temperature. Such TM reduction definitely must not happen in the bulk.

Conclusions

To summarize, we have demonstrated a simple method to construct high-quality Co_xB metallic glass infusion (beyond typical surface coating) of NCM secondary particles by reactive wetting. Under the strong driving force of interfacial chemical reaction, nanoscale Co_xB metallic glass not only completely wraps around the secondary-particle surfaces, but also infuses into the GBs between primary particles. This is extraordinary considering everything happens at room temperature, and the secondary particle has no alteration of the crystalline bulk, but with drastic changes in the GBs as they are infiltrated by reactive wetting. Consequently, it offers superior electrochemical performance (especially high-rate cycling stability at 7 C, high-temperature cycling at 45^{o}C, and impressive 95.0% capacity retention over 500 cycles in practical pouch-type full cells) and better safety by mitigating the entwinned cathode-side intergranular stress-corrosion cracking, microstructural degradation and side reactions, as well as transition-metal cross-over effect to the anode. Mechanistically, our atomistic simulations revealed the strong, selective interfacial bonding between Co_xB and NCM, which provides a consistent explanation of the reactive wetting and

suppressed oxygen activity observed experimentally. Reactive infusion of oxides by other transition-metal boride/phosphide/silicide metallic glasses, to produce “functional cermets”, should be a generic modification strategy for many electrodes used in advanced energy storage and conversion.

Methods

Synthesis

Hydroxide precursors of $LiNi_{0.8}Co_{0.1}Mn_{0.1}O_2$ (NCM) were synthesized by a co-precipitation method. Aqueous solution containing 3.2 M Ni^{2+}, 0.4 M Co^{2+}, and 0.4 M Mn^{2+} was prepared by dissolving nickel (II) sulfate hexahydrate ($NiSO_4 \cdot 6H_2O$), cobalt (II) sulfate heptahydrate ($CoSO_4 \cdot 7H_2O$), and manganese sulfate pentahydrate ($MnSO_4 \cdot 6H_2O$) with a molar ratio of 8:1:1. It was continuously fed into stirred tank reactor (4 L capacity) with 4.0 M sodium hydroxide (NaOH) and 0.4 M ammonia (NH_4OH) solutions under feeding rates of 300, 300, and 40 mL h^{-1}, respectively. A reaction temperature of 50°C was stably maintained by external water circulator for 20 h, after which hydroxide precursors were washed, collected, and dried at 110°C for 12 h. NCM811 was then synthesized by mixing hydroxide precursors (composition treated as $(Ni_{0.8}Co_{0.1}Mn_{0.1})(OH)_2$) with $LiOH \cdot H_2O$ with a molar ratio of 1:1.025, followed by a heat treatment first at 450°C for 2 h and then at 800°C for 10 h in flowing oxygen. To coat/infuse NCM811 with Co_xB compound, 100 mL anhydrous ethanol solution containing 0.009 M $Co(NO_3)_2 \cdot 6H_2O$ was first prepared under vacuum with Schlenk line to remove dissolved oxygen. 5.0 g NCM powders were next added under vigorous stirring under argon protection. Subsequently, 2 mL ethanol solution containing 0.078 M $NaBH_4$ was gradually added and maintained for 2 h under vigorous stirring under argon protection. The samples were then washed by anhydrous ethanol, collected by vacuum filtration, and dried at 120°C under vacuum overnight.

Material characterizations

Chemical compositions of cathode material and electrolyte were determined by an inductively coupled plasma optical emission spectrometer (ICP-OES, Varian 700-ES, Varian, Inc.). Phases and crystallographic structures were characterized by X-ray diffraction (XRD) using a parallel beam XRD instrument (Smartlab, Rigaku, with Cu Kα with wavelength of 1.542 Å). Specific surface areas were measured by a surface area and porosity analyzer (TriStar II, micromeritics) based on Brunauer–Emmett–Teller theory. Water content was measured by three times for each sample using Karl-Fischer Coulometric titration (Metrohm 831 KF Coulometer) and listed in **Supplementary Table 7**. Impurity contents (LiOH and Li_2CO_3) amounts were measured by an acid-based titration method[51] (Mettler Toledo Titrator) and listed in **Supplementary Table 8**. Briefly, 10 g cathode

powders were soaked into 100 ml deionized water. After stirring for 15 min, 40 mL clear solution is separated by a vacuum filtering and additional 100 mL deionized water was added. A flow of 0.1 M HCl is added to the solution under stirring, while pH of the solution was recorded. The experiments were considered finished when the pH of the solution reaches 4.0. *In situ* XRD measurements were conducted on cathodes assembled with a battery cell kit (Rigaku) in a glove box. After installing assembled battery cell kit on XRD stage, the cells were firstly cycled at 0.1C between 3.0~4.4V vs. Li/Li^+ as a formation step, after which, *in situ* XRD measurements were performed with Cu Kα radiation (Smartlab, Rigaku) during the charge process at a C-rate at 0.05 C between 3.0~4.4V vs. Li/Li^+. Cross-sections of cathodes and lithium metal anodes were cut by ion milling (IM-40000, Hitachi) and characterized under scanning electron microscopy (SEM, Verios 460, FEI) equipped with energy dispersive X-ray spectroscopy (EDS, XFlash® 6130, Bruker) detector. Morphologies and chemical compositions of the prepared cathode powders and electrodes were also characterized by SEM and EDS. Surface chemistry was analyzed by X-ray photon spectroscopy (XPS, Thermo Scientific Kα spectrometer). Before XPS measurements, all samples were rinsed by DMC solvent to remove residual electrolyte salt and by-products. *In situ* differential electrochemical mass spectrometry (DEMS) measurements were conducted on Swagelok type cells between 3.0 and 4.4 V (vs. Li/Li^+) with details described elsewhere[52]. For transmission electron microscopy (TEM) analysis, samples were prepared by dual-beam focused ion beam (FIB, Helios 450HP, FEI) using a 2-30 kV Ga ion beam. Prior to analysis in the FIB workstation, epoxy soaking, and carbon deposition were conducted to avoid damages of the Ga ion beam and preserve the sample morphology in subsequent lift-out and thinning processes. After lift-out, the prepared TEM samples were thinned to 200 nm using a 30 kV Ga ion beam. The thinned samples were next polished to remove surface contamination using Ar-ion milling system (Model 1040 Nanomill, Fischione) and immediately transferred and inspected under TEM. High-resolution TEM (HR-TEM, ARM300, JEOL) was conducted under 150 and 300 keV to collect scanning transmission electron microscopy (STEM) images for atomic and structural analysis. For elemental and spectrum analysis, electron energy loss spectroscopy (EELS) and energy dispersive X-ray spectroscopy (EDX) were conducted by HR-TEM (Aztec, Oxford). The thermal stability of charged cathodes was evaluated by differential scanning calorimeter (DSC; STAR 1, Mettler Toledo). The cathodes were firstly charged to 4.4 V (vs. Li/Li^+) at 0.1 C and then held at 4.4 V for additional 2 h. The cathode materials were

next collected from disassembled cells, rinsed with dimethyl carbonate to remove residual electrolytes and dried. 5.0 mg charged cathode powders were placed in a hermetic aluminum pan with 3 μl electrolyte. During DSC measurements, temperature was increased from the ambient condition to 400°C at a constant heating rate of 10 °C min^{-1}.

Electrochemical measurements

Composite cathodes were prepared by mixing 90 wt% active material, 5 wt% Super-P (as conductive agent), and 5 wt% poly(vinylidene fluoride) (as binder) in N-methyl-2-pyrrolidone (NMP). The slurry obtained was coated onto aluminum foil and dried at 120°C for 2 h. All cathodes for coin-type half cells were controlled with a loading level of 10.5±0.2 mg cm^{-2} (measured over five punched electrodes) and an electrode density of 3.20±0.03 g cm^{-3} (measured over five punched electrodes). Lithium metal batteries (LMBs) were assembled using 2032R coin-type cells in an argon glove box, with cathodes (diameter 14 mm), lithium metal foils (diameter 15 mm) as the counter and reference electrode, and 1.15 M $LiPF_6$ in ethylene carbonate/ethyl methyl carbonate/dimethyl carbonate with 5wt% fluoroethylene carbonate (EC:EMC:DMC = 3/4/3 vol% with 5% FEC) (Panax Starlyte) as the electrolyte (0.2 g added to each coin cell). All coin cells were evaluated with constant current-constant voltage mode between 3.0 and 4.4 V (vs. Li/Li^+) at 25/45°C. For all coin cells, the first charge-discharge cycle was conducted at 0.1 C. Here 1.0 C is defined as 220 mA g^{-1}. To evaluate the rate capability, the cells were charged at 0.5 C and discharged at various rates of 0.5, 1.0, 2.0, 3.0, 5.0, 7.0, and 10.0 C. After the rate testing, the cells were charged/discharged at 1.0 C with constant current (CC)–constant voltage (CV, 0.05 C cut-off) mode for another 100 cycles (41^{st}–140^{th} cycles in total number of cycling) to evaluate the cycling stability between 3.0 and 4.4 V (vs. Li/Li^+) at 25ºC. Galvanostatic intermittent titration technique (GITT) measurements were then conducted after the first (41^{st} cycle in total number of cycling) and last (140^{th} cycle in total number of cycling) cycles of 1.0 C cycling, between 3.0 and 4.4 V (vs. Li/Li^+) with a titration step at 0.5 C of 8 min and a relaxation step of 1 h. To evaluate the high-rate cycling stability, the cells were charged at 0.5 C and discharged at 5.0/7.0 C. After every 100 cycles, intermittent recovery step with charge/discharge rate of 0.2 C was conducted for 6 cycles. Electrochemical impedance spectroscopy (EIS) measurements were conducted on cells charged to 4.4 V (vs. Li/Li^+) from 1 MHz to 10 MHz and with AC voltage amplitude of 10 mV using VMP-

300 potentiostat (Bio-logic). Nickel-containing electrolyte were prepared by dissolving 0, 200, and 600 ppm nickel bis(trifluoromethane)sulfonimide $Ni(TFSI)_2$ in the base electrolyte (1.15 M $LiPF_6$ in EC:EMC:DMC = 3/4/3 vol%). Li/Li symmetric cells were assembled in the glove box with 80 μL of the prepared electrolyte for each cell. Galvanostatic cycling was performed on symmetric Li/Li cell at a Li plating/stripping current density of 1.0 or 2.0 mA cm^{-2} with a cycling capacity of 2.0 mAh cm^{-2} (2 h for each step). For full-cell tests, pristine NCM and Co_xB-NCM cathodes and spherical graphite (Gr) anodes were utilized to assemble 400 mAh-scale pouch-type full-cells. The ratio of negative to positive electrode capacity (N/P ratio) was fixed at 1.11 ± 0.01. The cathode loading level was 13.5 mg cm^{-2} on each side of the double-side coated Al foil. The anode loading level was 8.2 mg cm^{-2} on each side of the double-side coated Cu foil. The graphite electrode density was 1.44 g cm^{-3} and the cathode density was 3.35 g cm^{-3}. The pouch-type full-cells were assembled in a dry room with a humidity of less than 1%. The separator and liquid electrolyte are the same as those used in coin cells. The weight of electrolyte used in full cells is 1.0 g corresponding to 2.5 g Ah^{-1}. The cycling voltage window was at 2.8−4.3 V, and two formation cycle was conducted at 0.1 C before long-term cycling of 500 cycles at 1 C. Details for full-cell specifications are also listed in **Supplementary Table 9**. All electrochemical tests (except for EIS) were carried out using a TOSCAT-3100 battery cycler (TOYO SYSTEM).

Simulations

Spin-polarized first-principles calculations were conducted using Vienna *ab initio* simulation package (VASP) based on density functional theory (DFT) using the projector augmented-wave (PAW) method with Perdew-Burke-Ernzerhof (PBE) generalized gradient approximation (GGA)[53-55]. PAW potentials with $2s^1$ electron for Li, $3d^8 4s^2$ electrons for Ni, $2s^2 2p^4$ electrons for O, $3d^7 4s^2$ electrons for Co, and $2s^2 2p^1$ electrons for B were used. DFT+*U* was applied for 3*d* orbitals of Ni (*U*=6.0 eV and *J*=0 eV) and Co (*U*=3.4 eV and *J*=0 eV)[56, 57]. Plane-wave cutoff energy was set to be 520 eV and convergence was considered as reached when residue atomic forces were less than 0.05 eV/Å. (104) surface of layered $LiNiO_2$ was simulated by a supercell containing 20 Li, 20 Ni and 40 O, with two surfaces separated by a 10 Å vacuum layer. The Brillouin zone was sampled using Monhorst-Pack scheme with a 3×3×3 **k**-point mesh. Amorphous Co_xB was simulated by a supercell containing 70 Co and 32 B (corresponding to a composition close to $Co_{2.2}B$ measured

experimentally), and prepared by first-principles molecular dynamics at 2500 K for 3.0 ps followed by quenching and relaxation at 0 K. The Brillouin zone was sampled using Monhorst-Pack scheme with a 1×1×1 **k**-point mesh. To simulate the $Co_xB/LiNiO_2$ interface, an amorphous Co_xB slab containing 35 Co and 16 B were inserted between two (104) surfaces of a $LiNiO_2$ slab containing 20 Li, 20 Ni and 40 O. Their relative positions were adjusted so that the $Co_{35}B_{16}$ slab has a density is similar to that of the individually simulated amorphous Co_xB. The supercell was then heated to 2500 K for 3.0 ps or 12.0 ps by first-principles molecular dynamics (here the positions 20 Li, 20 Ni and 40 O were fixed to avoid the melting of $LiNiO_2$), followed by quenching and relaxation at 0 K. In all first-principles molecular dynamics calculations, the supercell size and shape were fixed and a time step of 1.5 fs was used. The Brillouin zone was sampled using Monhorst-Pack scheme with a 1×1×1 **k**-point mesh for first-principles molecular dynamics and a 2×3×2 **k**-point mesh for 0 K relaxation. The atomic structures were visualized and plotted using VESTA.[58] The projected density of states (DOS) of O 2*p* orbitals were summed over p_x, p_y, and p_z, including both spin-up and spin-down states.

Data availability. Data generated and analyzed in the present study are included in the manuscript and its Supplementary Information.

Acknowledgements

M.Y. and Y.D. contributed equally to this work. This work was supported by the Korea Institute of Energy Technology Evaluation and Planning (KETEP) and the Ministry of Trade, Industry & Energy (MOTIE) of the Republic of Korea (No. 20172410100140). 2020 Research Funds (1.200029.1) of Ulsan National Institute of Science and Technology (UNIST) is also greatly acknowledged. Y.D. and J.L. acknowledge support by the Department of Energy, Basic Energy Sciences, under award number DE-SC0002633 (Chemomechanics of Far-From-Equilibrium Interfaces).

Author contributions

M.Y., Y.D., J.L., and J.C. conceived the project. M.Y. synthesized the materials and conducted electrochemical testing. Y.D. conducted simulations and theoretical analysis. M.Y. and J.H.

conducted *ex-*/*in-situ* XRD measurements and analysis. H.C. and J.S. conducted focused ion beam, TEM, SEM and XPS measurements. S.J.K. provided equipment for DEMS measurements. M.Y. and K.A. assembled and tested pouch-type full cells. M.Y. and Y.D. analyzed the data. M.Y., Y.D., J.L., and J.C. wrote the paper. All authors discussed and contributed to the writing.

Competing interests

The authors declare no competing interests.

References

1 Nitta, N., Wu, F., Lee, J. T. & Yushin, G. Li-ion battery materials: present and future. *Mater. Today* **18**, 252-264 (2015).

2 Kim, J. *et al.* Prospect and Reality of Ni-Rich Cathode for Commercialization. *Adv. Energy Mater.* **8**, 1702028 (2018).

3 Li, W., Erickson, E. M. & Manthiram, A. High-nickel layered oxide cathodes for lithium-based automotive batteries. *Nat. Energy* **5**, 26-34 (2020).

4 Edström, K., Gustafsson, T. & Thomas, J. O. The cathode–electrolyte interface in the Li-ion battery. *Electrochim. Acta* **50**, 397-403 (2004).

5 Sharifi-Asl, S., Lu, J., Amine, K. & Shahbazian-Yassar, R. Oxygen Release Degradation in Li-Ion Battery Cathode Materials: Mechanisms and Mitigating Approaches. *Adv. Energy Mater.* **9**, 1900551 (2019).

6 Xie, Q., Li, W. & Manthiram, A. A Mg-Doped High-Nickel Layered Oxide Cathode Enabling Safer, High-Energy-Density Li-Ion Batteries. *Chem. Mater.* **31**, 938-946 (2019).

7 Schipper, F. *et al.* From Surface ZrO_2 Coating to Bulk Zr Doping by High Temperature Annealing of Nickel-Rich Lithiated Oxides and Their Enhanced Electrochemical Performance in Lithium Ion Batteries. *Adv. Energy Mater.* **8**, 1701682 (2018).

8 Xu, X. *et al.* Radially Oriented Single-Crystal Primary Nanosheets Enable Ultrahigh Rate and Cycling Properties of $LiNi_{0.8}Co_{0.1}Mn_{0.1}O_2$ Cathode Material for Lithium-Ion Batteries. *Adv. Energy Mater.* **9**, 1803963 (2019).

9 Kim, J. *et al.* A highly stabilized nickel-rich cathode material by nanoscale epitaxy control for high-energy lithium-ion batteries. *Energy Environ. Sci.* **11**, 1449-1459 (2018).

10 Yan, P. *et al.* Tailoring grain boundary structures and chemistry of Ni-rich layered cathodes for enhanced cycle stability of lithium-ion batteries. *Nat. Energy* **3**, 600-605 (2018).

11 Xu, G.-L. *et al.* Building ultraconformal protective layers on both secondary and primary particles of layered lithium transition metal oxide cathodes. *Nat. Energy* **4**, 484-494 (2019).

12 Li, L. *et al.* Hidden Subsurface Reconstruction and Its Atomic Origins in Layered Oxide Cathodes. *Nano Lett.* **20**, 2756-2762 (2020).

13 Liu, H. *et al.* Intergranular Cracking as a Major Cause of Long-Term Capacity Fading of Layered Cathodes. *Nano Lett.* **17**, 3452-3457 (2017).

14 Yan, P. *et al.* Coupling of electrochemically triggered thermal and mechanical effects to aggravate failure in a layered cathode. *Nat. Commun.* **9**, 2437 (2018).

15 Watanabe, S., Kinoshita, M., Hosokawa, T., Morigaki, K. & Nakura, K. Capacity fade of $LiAl_yNi_{1-x-y}Co_xO_2$ cathode for lithium-ion batteries during accelerated calendar and cycle life tests (surface analysis of $LiAl_yNi_{1-x-y}Co_xO_2$ cathode after cycle tests in restricted depth of discharge ranges). *J. Power Sources* **258**, 210-217 (2014).

16 Jung, R., Metzger, M., Maglia, F., Stinner, C. & Gasteiger, H. A. Chemical versus Electrochemical Electrolyte Oxidation on NMC111, NMC622, NMC811, LNMO, and Conductive Carbon. *J. Phys. Chem. Lett.* **8**, 4820-4825 (2017).

17 Freiberg, A. T. S., Roos, M. K., Wandt, J., de Vivie-Riedle, R. & Gasteiger, H. A. Singlet Oxygen Reactivity with Carbonate Solvents Used for Li-Ion Battery Electrolytes. *J. Phys. Chem. A* **122**, 8828-8839 (2018).

18 Zhan, C., Wu, T., Lu, J. & Amine, K. Dissolution, migration, and deposition of transition metal ions in Li-ion batteries exemplified by Mn-based cathodes – a critical review. *Energy Environ. Sci.* **11**, 243-257 (2018).

19 Huang, Y. *et al.* Lithium Manganese Spinel Cathodes for Lithium-Ion Batteries. *Adv. Energy Mater.* 2000997 (2020).

20 Zhu, Z. *et al.* Gradient Li-rich oxide cathode particles immunized against oxygen release by a molten salt treatment. *Nat. Energy* **4**, 1049-1058 (2019).

21 Yan, P. *et al.* Injection of oxygen vacancies in the bulk lattice of layered cathodes. *Nat. Nanotechnol.* **14**, 602-608 (2019).

22 Armstrong, A. R. *et al.* Demonstrating Oxygen Loss and Associated Structural Reorganization in the Lithium Battery Cathode $Li[Ni_{0.2}Li_{0.2}Mn_{0.6}]O_2$. *J. Am. Chem. Soc.* **128**, 8694-8698 (2006).

23 House, R. A. *et al.* What Triggers Oxygen Loss in Oxygen Redox Cathode Materials? *Chem. Mater.* **31**, 3293-3300 (2019).

24 Yoon, M. *et al.* Unveiling Nickel Chemistry in Stabilizing High-Voltage Cobalt-Rich Cathodes for Lithium-Ion Batteries. *Adv. Funct. Mater.* **30**, 1907903 (2020).

25 Jain, A. *et al.* Commentary: The Materials Project: A materials genome approach to accelerating materials innovation. *APL Mater.* **1**, 011002 (2013).

26 Mu, D., Yang, C., Shen, B.-l. & Jiang, H. Oxidation resistance of borided pure cobalt. *J. Alloys Compd.* **479**, 629-633 (2009).

27 Yang, Y., Kushima, A., Han, W., Xin, H. & Li, J. Liquid-Like, Self-Healing Aluminum Oxide during Deformation at Room Temperature. *Nano Lett.* **18**, 2492-2497 (2018).

28 Li, J., Lenosky, T. J., Först, C. J. & Yip, S. Thermochemical and Mechanical Stabilities of the Oxide Scale of ZrB_2+SiC and Oxygen Transport Mechanisms. *J. Am. Ceram. Soc.* **91**, 1475-1480 (2008).

29 R. Hasegawa & R. Ray. Iron-boron metallic glasses. *J. Appl. Phys.* **49**, 4174-4179 (1978).

30 P. H. Gaskell. A new structural model for amorphous transition metal silicides, borides, phosphides and carbides. *J. Non-Cryst. Solids* **32**, 207-224 (1979).

31 Masa, J. *et al.* Amorphous Cobalt Boride (Co_2B) as a Highly Efficient Nonprecious Catalyst for Electrochemical Water Splitting: Oxygen and Hydrogen Evolution. *Adv. Energy Mater.* **6**, 1502313 (2016).

32 Deng, J. *et al.* Co–B Nanoflakes as Multifunctional Bridges in $ZnCo_2O_4$ Micro-/Nanospheres for Superior Lithium Storage with Boosted Kinetics and Stability. *Adv. Energy Mater.* **9**, 1803612 (2019).

33 Jiang, B. *et al.* A mesoporous non-precious metal boride system: synthesis of mesoporous cobalt boride by strictly controlled chemical reduction. *Chem. Sci.* **11**, 791-796 (2020).

34 Chen, Z. *et al.* Study of cobalt boride-derived electrocatalysts for overall water splitting. *Int. J. Hydrog. Energy* **43**, 6076-6087 (2018).

35 Zhang, C. *et al.* Revealing the role of NH_4VO_3 treatment in Ni-rich cathode materials with improved electrochemical performance for rechargeable lithium-ion batteries. *Nanoscale* **10**, 8820-8831 (2018).

36 Yu, Y. *et al.* Optimal annealing of Al foil anode for prelithiation and full-cell cycling in Li-ion battery: The role of grain boundaries in lithiation/delithiation ductility. *Nano Energy* **67**, 104274 (2020).

37 Miller, D. J., Proff, C., Wen, J. G., Abraham, D. P. & Bareño, J. Observation of Microstructural Evolution in Li Battery Cathode Oxide Particles by In Situ Electron Microscopy. *Adv. Energy Mater.* **3**, 1098-1103 (2013).

38 Kondrakov, A. O. *et al.* Anisotropic Lattice Strain and Mechanical Degradation of High- and Low-Nickel NCM Cathode Materials for Li-Ion Batteries. *J. Phys. Chem. C* **121**, 3286-3294 (2017).

39 Kim, J. *et al.* Controllable Solid Electrolyte Interphase in Nickel-Rich Cathodes by an Electrochemical Rearrangement for Stable Lithium-Ion Batteries. *Adv. Mater.* **30**, 1704309 (2018).

40 Zhao, W. *et al.* High Voltage Operation of Ni-Rich NMC Cathodes Enabled by Stable Electrode/Electrolyte Interphases. *Adv. Energy Mater.* **8**, 1800297 (2018).

41 Yoon, W.-S. *et al.* Investigation of the Charge Compensation Mechanism on the Electrochemically Li-Ion Deintercalated $Li_{1-x}Co_{1/3}Ni_{1/3}Mn_{1/3}O_2$ Electrode System by Combination of Soft and Hard X-ray Absorption Spectroscopy. *J. Am. Chem. Soc.* **127**, 17479-17487 (2005).

42 Lin, F. *et al.* Profiling the nanoscale gradient in stoichiometric layered cathode particles for lithium-ion batteries. *Energy Environ. Sci.* **7**, 3077-3085 (2014).

43 Yang, L., Ravdel, B. & Lucht, B. L. Electrolyte Reactions with the Surface of High Voltage $LiNi_{0.5}Mn_{1.5}O_4$ Cathodes for Lithium-Ion Batteries. *Electrochem. Solid-State Lett.* **13**, A95-A97 (2010).

44 Zheng, J. *et al.* Highly Stable Operation of Lithium Metal Batteries Enabled by the Formation of a Transient High-Concentration Electrolyte Layer. *Adv. Energy Mater.* **6**, 1502151 (2016).

45 Li, W. *et al.* Dynamic behaviour of interphases and its implication on high-energy-density cathode materials in lithium-ion batteries. *Nat. Commun.* **8**, 14589 (2017).

46 Nguyen, T. T. D. *et al.* Understanding the Thermal Runaway of Ni-Rich Lithium-Ion Batteries. *World Electr. Veh. J.* **10**, 79 (2019).

47 Lin, D., Liu, Y. & Cui, Y. Reviving the lithium metal anode for high-energy batteries. *Nat. Nanotechnol.* **12**, 194-206 (2017).

48 Seo, D.-H. *et al.* The structural and chemical origin of the oxygen redox activity in layered and cation-disordered Li-excess cathode materials. *Nat. Chem.* **8**, 692-697 (2016).

49 Luo, K. *et al.* Charge-compensation in 3d-transition-metal-oxide intercalation cathodes through the generation of localized electron holes on oxygen. *Nat. Chem.* **8**, 684-691 (2016).

50 Hashigami, S. *et al.* Improvement of Cycleability and Rate-Capability of

$LiNi_{0.5}Co_{0.2}Mn_{0.3}O_2$ Cathode Materials Coated with Lithium Boron Oxide by an Antisolvent Precipitation Method. *Chemistry Select* **4**, 8676-8681 (2019).

51 Park, J.-H. *et al.* Effect of Residual Lithium Rearrangement on Ni-rich Layered Oxide Cathodes for Lithium-Ion Batteries. *Energy Technol.* **6**, 1361-1369 (2018).

52 Kang, S. J., Mori, T., Narizuka, S., Wilcke, W. & Kim, H.-C. Deactivation of carbon electrode for elimination of carbon dioxide evolution from rechargeable lithium–oxygen cells. *Nat. Commun.* **5**, 3937 (2014).

53 Kresse, G. & Joubert, D. From Ultrasoft Pseudopotentials to the Projector Augmented-Wave Method. *Phys. Rev. B: Condens. Matter Mater. Phys.* **59**, 1758 (1999).

54 Kresse, G. & Furthmüller, J. Efficiency of ab-initio total energy calculations for metals and semiconductors using a plane-wave basis set. *Comput. Mater. Sci.* **6**, 15-50 (1996).

55 Perdew, J. P., Burke, K. & Ernzerhof, M. Generalized Gradient Approximation Made Simple. *Phys. Rev. Lett.* **77**, 3865-3868 (1996).

56 Dudarev, S. L., Botton, G. A., Savrasov, S. Y., Humphreys, C. J. & Sutton, A. P. Electron-energy-loss spectra and the structural stability of nickel oxide: An LSDA+U study. *Phys. Rev. B* **57**, 1505-1509 (1998).

57 Jain, A. *et al.* Formation enthalpies by mixing GGA and GGA +U calculations. *Phys. Rev. B* **84**, 045115 (2011).

58 Momma, K. & Izumi, F. VESTA 3 for Three-dimensional Visualization of Crystal, Volumetric and Morphology Data. *J. Appl. Crystallogr.* **44**, 1272-1276 (2011).